Ceramics International 49 (2023) 41201–41209

Contents lists available at ScienceDirect

Ceramics International

journal homepage: www.elsevier.com/locate/ceramint

Er/Yb co-doped $LiYF_4$ transparent oxyfluoride glass-ceramics with up-conversion optical properties

N.M.P. Truong [a], M. Sedano [b], A. Durán [b], R. Balda [c,d], M.J. Pascual [b,*], R. Klement [a]

[a] Centre for Functional and Surface Functionalized Glass (FUNGLASS), Alexander Dubček University of Trenčín Študentská 2, 91150, Trenčín, Slovakia
[b] Ceramics and Glass Institute (CSIC), C/Kelsen 5, Campus de Cantoblanco, 28049, Madrid, Spain
[c] Departamento Física Aplicada, Escuela Superior de Ingeniería, Universidad del País Vasco (UPV-EHU), Bilbao, Spain
[d] Centro de Física de Materiales CFM, (UPV/EHU-CSIC), San Sebastian, Spain

ARTICLE INFO

Handling Editor: Dr P. Vincenzini

Keywords:
$LiYF_4$
Oxyfluoride glasses
Up-conversion photoluminescence
Rare earth ions
Transparent glass-ceramics

ABSTRACT

Transparent oxyfluoride glass-ceramics doped with rare earth ions (RE^{3+}) are promising materials for photoluminescence up- and down-conversion. In this study, glass compositions within the system $40SiO_2$–$25Al_2O_3$–$18Li_2O$–$7LiF$–$10YF_3$ (mol.%) doped with ErF_3 and codoped with ErF_3/YbF_3 were prepared by melt-quenching method and subjected to thermal treatment at temperatures above glass transition (T_g + 35 °C) for long dwell times to obtain the corresponding glass-ceramics. The formation of $LiYF_4$ and $LiAlSiO_4$ nanocrystals was confirmed by XRD analysis after thermal treatment at 540 °C for 20 h. The increase in the treatment time up to 80 h resulted in the enhancement of the UC luminescence yield and the decrease of the Red to Green ratio (R/G) emission intensity. Due to the nano-sized crystals, the glass-ceramic products were transparent (%T) in near-infrared (NIR) and visible spectral region with %T remaining approximately 85% and 75%, respectively, after 20 h treatment. However, the visible window transparency reduced, with %T dropping to around 50% after 80 h due to the increase in crystal size and crystalline fraction. The influence of Yb^{3+} co-doping on the up-conversion (UC) luminescence has been investigated in the glass-ceramics and compared to the parent glasses, confirming that Yb^{3+} ions were also a key factor for facilitating up-conversion via energy transfer (ET), leading to a greater luminescence yield than for Er^{3+} single doped glass-ceramics and tuning of R/G intensities.

1. Introduction

Glass-ceramics (GCs) are materials in which crystals are embedded in a glass matrix. Crystallization from an amorphous state is a remarkable process due to the fact that nucleation and growth rate act to tailor diverse physical properties, including thermal, mechanical, electrical, and optical capabilities [1–3]. Particularly, transparent oxyfluoride glass-ceramics (TGCs) doped with rare earth ions (RE^{3+}) are one of the most favorable groups of materials for high efficiency up- and down-conversion photoluminescence (PL) emission. They are well-suited for using in optoelectronics and optical refrigeration because of their transparency, mechanical and chemical resistance, low phonon energies and low refractive index inherited from fluoride crystals [4–7]. In order to achieve transparency, the crystal size, morphology, isotropic crystalline phases and their homogeneous distribution in glass matrix need to be strictly controlled [8]. The luminescence yield of the GCs is enhanced by regulating oriented crystallization in fluoride phases after heat treatment, hence achieving single-crystal-like characteristics [9]. Oxide glasses have substantially higher phonon energy ($h\upsilon_{ph} \approx 1100$ cm^{-1}) than fluoride glasses ($h\upsilon_{ph} \approx 550$ cm^{-1}) so, energy quenching via vibrational relaxation occurred. Fluoride glasses, on the other hand, can prevent energy loss via vibrational relaxation due to their low phonon energy, but they are chemically and mechanically unstable [1]. The GCs are viewed as gap fillers that can compensate for the deficiencies of both materials. In particular, the $LiYF_4$ phase considered for this study, possess a low phonon energy, $h\upsilon_{ph} = 446$ cm^{-1} [10,11].

Due to the potential light emission features of fluoride phases, crystallization of RE^{3+} doped $AREF_4$ (A, alkali metals) in oxyfluoride glass-ceramics (OxGCs) has been intensively studied. A. De Pablos et al. [12] investigated $KLaF_4$ transparent GCs containing both cubic and hexagonal crystals with very low phonon energy ($h\upsilon_{ph} \approx 262$ cm^{-1}) and provided a promising look at scientific background for future researches in terms of enhanced photoluminescence. A. de Pablos et al. [13] also reported the optical properties of GCs based on hexagonal $NaYF_4$:Er^{3+}

* Corresponding author.
E-mail address: mpascual@icv.csic.es (M.J. Pascual).

https://doi.org/10.1016/j.ceramint.2023.05.142
Received 29 March 2023; Received in revised form 9 May 2023; Accepted 15 May 2023
Available online 20 May 2023

nanocrystals. The PL of the investigated GCs was ten times higher than that of the parent glass, with predominating green emission (550 nm) and a lower intensity of red emission (670 nm). Er^{3+} dopant ions were incorporated into the $NaYF_4$ nanocrystals during the crystallization process, as indicated by the time-dependent sharpening of the stark-split structure in the GCs. The incorporation of Yb^{3+} in Er^{3+}/Yb^{3+}-co-doped OxGCs significantly improved the optical properties that governed the efficiency of light emission. However, co-doped samples exhibited a stronger red UC emission than the green emission, in contrast to those with only Er^{3+} doping. The intensity ratio of green and red UC emissions could be governed by the crystalline fraction and adjusted with the Er/Yb ratio [13–15]. Cabral et al. [16] claimed the formation of cubic (α-phase) and hexagonal (β-phase) $KLaF_4$ NCs from the glasses $70SiO_2$–$7Al_2O_3$–$16K_2O$–$7LaF_3$:xNdF_3 (mol.%, x = 0.1–2%) after heat treatment at T_g + 10–100 °C, highlighting the distinguishable growth kinetics of the two phases. After 15 h of treatment at 660 °C with 0.5% Nd^{3+} dopant, the formation of dominated β-$KLaF_4$ resulted in superior PL emission compared to the α-phase alone. From the same aspect, J. Qiu et al. [17] investigated the cubic-to-hexagonal phase transformation of $NaYF_4$ in the system $40SiO_2$-(10+x)ZnO-(33-x)Na_2CO_3–$10YF_3$–7NaF-0.1TbF_3-0.5YbF_3x; with x = 0, 5, 10, 15 (mol.%). The goal was to improve UC emission by modifying the ZnO/Na_2O ratio and integrating Tb^{3+}-Yb^{3+} ions into the crystal phases of transparent Zincatesilion oxyfluoride glasses and OxGCs. They discovered that adding 10–15 mol.% ZnO produced a pure cubic phase, while adding 20 mol.% ZnO generated a mixture of cubic and hexagonal phases. When the ZnO concentration reached 25 mol.%, the pure hexagonal phase was formed. Because the crystal field symmetry of hexagonal β-$NaYF_4$ phase was lower than that of the cubic α- $NaYF_4$, the absorptive capacity of RE^{3+} ions and the dipole polarizability of RE^{3+} ions were both increased [17].

With the smaller cationic radius compared to Na^+/K^+, and higher cation polarization power, the substitution of Li^+ can cause crystal field distortion and increase the asymmetry environment around the trivalent lanthanide ions, forming scheelite-type tetragonal (bipyramidal) instead of hexagonal or cubic phases. Therefore, it significantly affects the emission intensity as reported recently [9]. Notably, $LiYF_4$ crystal is a suitable host for trivalent RE^{3+} ions because their similar ionic radii can provide high capacity for isomorphic replacement of Y^{3+} ions by other RE^{3+} ions with negligible influence on the lattice structure [9,18]. J. Qiu et al. [19] studied $40SiO_2$–$20Al_2O_3$–20LiF-20GdF_3 TGC system, singly doped with 1 at. % Eu^{3+}, 1 at. % Tb^{3+} and 1 at. % Tm^{3+} ions, respectively. They confirmed the inverse scheelite structure of the $LiGdF_4$ crystalline phase, with nanocrystals of size around 20–50 nm. The low symmetry sites around the RE^{3+} ions significantly prolonged fluorescence lifetime via electric dipole transitions. Recent research conducted by X. Li and his team [20] uncovered the co-precipitation of tetragonal $LiYF_4$ and hexagonal $LiAlSiO_4$ in $40SiO_2$–$25Al_2O_3$–$5Li_2O$–20KF–$10YF_3$ because of the excess Li^+ ions. The sample containing 5 mol.% of Na_2O or K_2O in the glass batch composition produced pure $LiYF_4$ NCs since the Na^+/K^+ functioned as bond breakers and facilitated the presence of Li^+ in the glass matrix.

Based on prior research findings, the goal of this work is to produce RE-doped transparent GCs incorporating lithium fluoride phases, specifically scheelite-type tetragonal $LiYF_4$ nanoparticles, using the melt-quenching method and subsequent thermal treatment to improve luminescence yield and prolong emission lifetime.

2. Experimental

2.1. Glasses and glass-ceramics preparation

High purity silica nano-powders (SiO_2, 99.9%, Alfa Aesar), aluminum oxide (Al_2O_3, 99.99%, Alfa Aesar), yttrium fluoride (YF_3, 99.9%, Alfa Aesar), lithium carbonate (Li_2CO_3, 99.998%, Alfa Aesar), lithium fluoride (LiF, 99.98%, Alfa Aesar), ytterbium fluoride (YbF_3, 99.99%, Alfa Aesar), and erbium fluoride (ErF_3, 99.9%, Alfa Aesar) were used as raw materials for glasses preparation.

A series of glasses with the composition $40SiO_2$–$25Al_2O_3$–$18Li_2O$–7LiF-(10-x-y)YF_3-xEr_3-yYbF_3 (in mol.%.), in which YF_3 was partially substituted by ErF_3 and YbF_3, were produced by melt-quenching method. The theoretical composition of glasses and corresponding sample notations are summarized in Table 1. Batches of 50 g of each composition were homogenized for 1 h prior to melting in a Pt/Rh crucible covered with a lid to prevent fluorine and lithium evaporation in an electric furnace. First, the batches were held at 1200 °C for 1 h and calcined. Then, the temperature was gradually increased to 1500 °C with a heating rate of 10 °C/min, and the formed melt was homogenized and held for an additional hour prior to the first casting. To improve the homogeneity of the prepared glass, the formed glass was re-melted for 1/2 h at the same melting temperature, 1500 °C. The glass melt was casted on a brass mold and annealed in a furnace at temperature T_g + 5 °C for 0.5 h to relieve residual stresses. The annealed glass was then progressively cooled down at 1 °C/min to ambient temperature.

The GC samples were prepared using the following procedure: the corresponding glasses were cut into pieces and subjected to heat treatment in a furnace at a temperature of 540 °C (around T_g + 35 °C) with selected dwell times of 20, 40, and 80 h, respectively. The heating ramp from RT to 540 °C was 10 °C/min; and for sample cooling, a rate of 2 °C/min was used. The heat treatment temperature was chosen based on the thermal behavior of the prepared glasses (DTA analysis, see text below); the working temperature was high enough, above T_g, to promote crystallization of nano-crystalline fluoride phases but low enough, under T_x to avoid uncontrollable crystallization and loss of transparency of prepared GCs.

In this study, chemical compositions were determined with a Magic X 2400 (PANalytical) spectrometer in order to track chemicals, specifically fluorine loss. To prepare the beads for analysis, 0.3 g of sample was combined with 5.5 g of lithium tetraborate ($Li_2B_4O_7$) and melted at 1100 °C. Utilizing the IQ + software, the calculation was performed (PANalytical).

2.2. Thermal and structural characterization

Differential Thermal Analysis (DTA/TG, Netzsch STA 409/C, Germany) was used to investigate the glass thermal properties and to estimate glass transition temperature (T_g), the onset of crystallization (T_x) and crystallization temperature (T_p). The DTA/TG traces were recorded in the temperature range of 25–1000 °C at the heating rate of 10 °C/min in air atmosphere. The powdered glass samples 20–30 mg with the grain size of 1–1.25 μm and powdered Al_2O_3 as an inert reference material were used for the analysis.

X-ray diffraction (XRD) measurements were conducted by an X-ray diffractometer (D8 ADVANCE, Bruker, USA) equipped with a Lynx Eye detector. The diffractograms were collected using monochromatic CuKα$_1$ radiation (1.54056 Å) in the $5° \leq 2\theta \leq 70°$ range with a step of 0.05°/sec. The crystalline phases were identified and analyzed using EVA Difrac PLUS software (V2, Karlsruhe, Germany). The mean crystallite sizes were estimated by Scherer's equation:

$$D = \frac{k\lambda}{\sqrt{\beta_m^2 - \beta_i^2} * \cos\theta} \quad (1)$$

where D is the mean size of the crystallite domain, k is the shape

Table 1
Chemical compositions (in mol.%) of the oxyfluoride glasses.

Sample's code	Composition (mol.%)
Undoped glass	$40SiO_2$–$25Al_2O_3$–$18Li_2O$–7LiF–$10YF_3$
G0.1Er-0.4 Yb	$40SiO_2$–$25Al_2O_3$–$18Li_2O$–7LiF-9.5YF_3-0.1ErF_3-0.4YbF_3
G0.5Er	$40SiO_2$–$25Al_2O_3$–$18Li_2O$–7LiF-9.5YF_3-0.5ErF_3
G0.5Er-2Yb	$40SiO_2$–$25Al_2O_3$–$18Li_2O$–7LiF-7.5YF_3-0.5ErF_3-2YbF_3
G0.5Er-4Yb	$40SiO_2$–$25Al_2O_3$–$18Li_2O$–7LiF-5.5YF_3-0.5ErF_3-4YbF_3

factor selected as 0.94, generally due to $LiYF_4$ scheelite structure, λ is the wavelength of X-rays (0.154056 nm), θ is the Bragg angle X-ray diffraction peak, β_m is the line broadening at half the maximum intensity (FWHM) of the measured peak, and β_i is the line broadening at FWHM of the standard powder NaF (PROVYS 99.9%) to include the instrument response function. The pseudo-Voight profile function was used in the Rietveld refinement of the recorded XRD diffractograms.

High resolution transmission electron microscopy (HR-TEM) was used to confirm the crystals morphology in the GCs. The glass G0.5Er-4Yb and its corresponding GC treated at 540 °C for 80 h were crushed into powder (<60 μm) and dispersed in ethanol. The micrographs were taken with a JEOL-JEM 2100 HT (Japan) equipped with a thermionic cathode electron gun and LaB6 filament working at 200 kV with a 0.19 nm resolution. ImageJ software was used for micrograph analysis.

2.3. Optical characterization

The polished samples of 1 mm thickness were used for optical characterization. The refractive indices of doped-glass samples (1 mm thickness), were measured by ellipsometry with a Gaertner 117 equipment, operated by the HeNe laser using the 632.8 nm wavelength to record the refractive indices.

Ultraviolet–Visible (UV–Vis) spectroscopy (Cary 5000, Agilent Technologies USA) was applied to determine the transmittance of samples in the spectral range of 190–2000 nm.

The up-conversion photoluminescence (UC-PL) spectra, corrected for the spectrometer response, were recorded using a Fluorolog FL3-21 (Horiba, France) spectrometer. A continuous-wave diode laser operating at a wavelength of 980 nm was used as an excitation source; and an excitation power of 500 mW was applied to record all up-conversion PL spectra. The decay curves were recorded at RT on the same instrument using a pulsed Deltadiode (DD-375 L, Horiba, France, peak wavelength 376 nm, pulse duration 50ps, repetition rate 10 kHz-100 MHz) at 376 nm as an excitation source; the green (~540 nm) and red (~665 nm) emission wavelengths were monitored. The decay curves were fitted using a double-exponential function.

3. Results and discussion

The undoped parent glass was colorless and transparent. The doped glasses were light pink and transparent due to the presence of ErF_3. The fluorine and lithium loss, as determined by X-ray Fluorescence (XRF), was found to be in the range of 20% and 40%, respectively. The refractive indices of four glass samples with varying dopant concentrations were only slightly different, according to Table 2. All glass samples showed similar results for refractive indices, demonstrating that the partial substitution of Y^{3+} with Er^{3+} and Yb^{3+} ions had little effect on the lattice structures.

Fig. 1 and Table 2 showed in detail that the T_g of all glass samples were approximately 505 °C. The T_x value ranged from approximately 605 to 685 °C as the dopant concentration increased. The increase in T_x expanded the thermal stability of the glasses from approximately 100 to 180 °C. To avoid opalescence, the ceramization temperature (T_c) range was selected as $T_g < T_c < T_x$, in which T_c for preparing OxGCs in this study was set at 540 °C, (~ T_g + 35 °C). The working intervals were set to 20, 40, and 80 h; the ramp up rate was 10 °C/min, and the ramp down rate was 2 °C/min. Due to the optical emission yield interest of these glasses and their GCs, the crystallization experiments were undertaken solely on the four doped glasses.

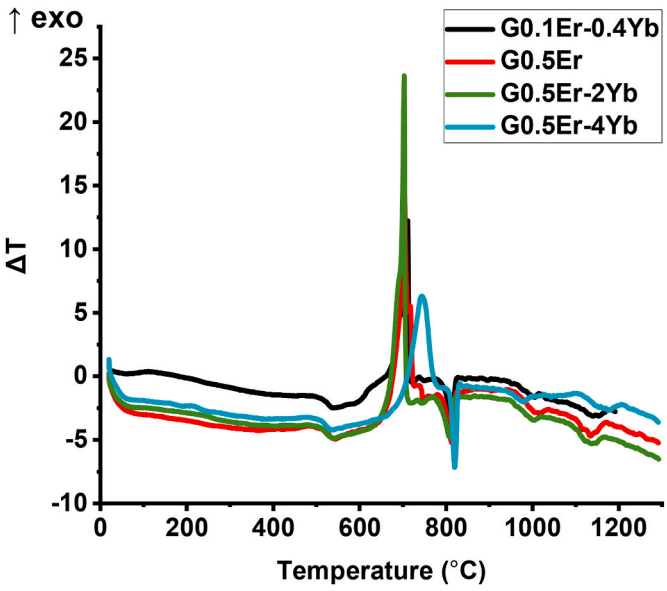

Fig. 1. DTA traces of the doped glasses recorded at 10 °C/min in air atmosphere.

The XRD patterns of the parent glasses (not shown) revealed the typical amorphous halo without any indication of diffraction peaks, thus confirming the fully amorphous nature of the as prepared glasses. After 20 h of treatment at 540 °C, the initial targeted peak of the $LiYF_4$ phase was clearly apparent in Fig. 2a. As the duration of heat treatment increased, the XRD diffraction peaks in all samples became more better defined, indicating that body-centered tetragonal $LiYF_4$ crystals (JCPDS no. 00-017-0874) were gradually formed (Fig. 2 a, b, c). The Rietveld analysis was in good agreement with the experimental pattern, confirming the formation of $LiYF_4$ with the calculated lattice parameters, a = b = 5.168 Å and c = 10.736 Å, similar to those obtained for the corresponding bulk materials, a = b = 5.164 Å, c = 10.741 Å [21]. The semi-quantitative analysis of the XRD patterns for the sample G0.5Er-4Yb treated at different dwell times revealed $LiYF_4$ crystal fraction of about 7, 9 and 13 wt% for 20, 40 and 80 h, respectively. The crystal size of the precipitated $LiYF_4$ phase was calculated using Scherer's equation (Eqn. (1)). Maintaining the same treatment temperature, after 80 h, the nano-$LiYF_4$ in the doped-OxGCs were around 10–13 nm, Fig. 2c, based on an evolution of $LiYF_4$ by treatment time. This could be explained by the effect of a diffusive barrier containing network formers such as silica or alumina around the $LiYF_4$ nanocrystals which inhibits crystal growth. The peaks at 2θ = 29.5 of GC0.1Er-0.4 Yb and GC0.5Er in Fig. 2b were slightly shifted into larger angles at 2θ = 29.56/29.49628 and 2θ = 29.58 of GC0.5Er-2Yb and GC0.5Er-4Yb, respectively. The larger 2θ angles shift could be the result of the shrinkage in nanocrystal lattice by substituting larger Y^{3+} (ionic radius: 1.019 Å) with smaller trivalent ions Er^{3+} (ionic radius: 1.004 Å) and Yb^{3+} (ionic radius: 0.985 Å), respectively [22].

The additional crystals of $LiAlSiO_4$, in hexagonal morphology (JCPDS no. 00-045-0466), gained a growth advantage with time and were approximately 16 nm in size after 80 h of treatment, Fig. 2d. Unlike $LiYF_4$, these crystals became the primary factor in reducing the sample's transparency.

Table 2
Characteristic temperatures, T_g, T_x, ΔT, T_p estimated from DTA traces and refractive index of doped- and undoped-glasses.

Sample's code	$T_g \pm 2$ (°C)	$T_x \pm 2$ (°C)	ΔT (°C)	$T_p \pm 2$ (°C)	Refractive index ±0.003
Undoped glass	511	592	81	640	1.576
G 0.1Er-0.4 Yb	504	604	100	711	1.551
G 0.5Er	505	660	157	703	1.546
G 0.5Er-2Yb	502	648	146	703	1.553
G 0.5Er-4Yb	505	686	181	713	1.550

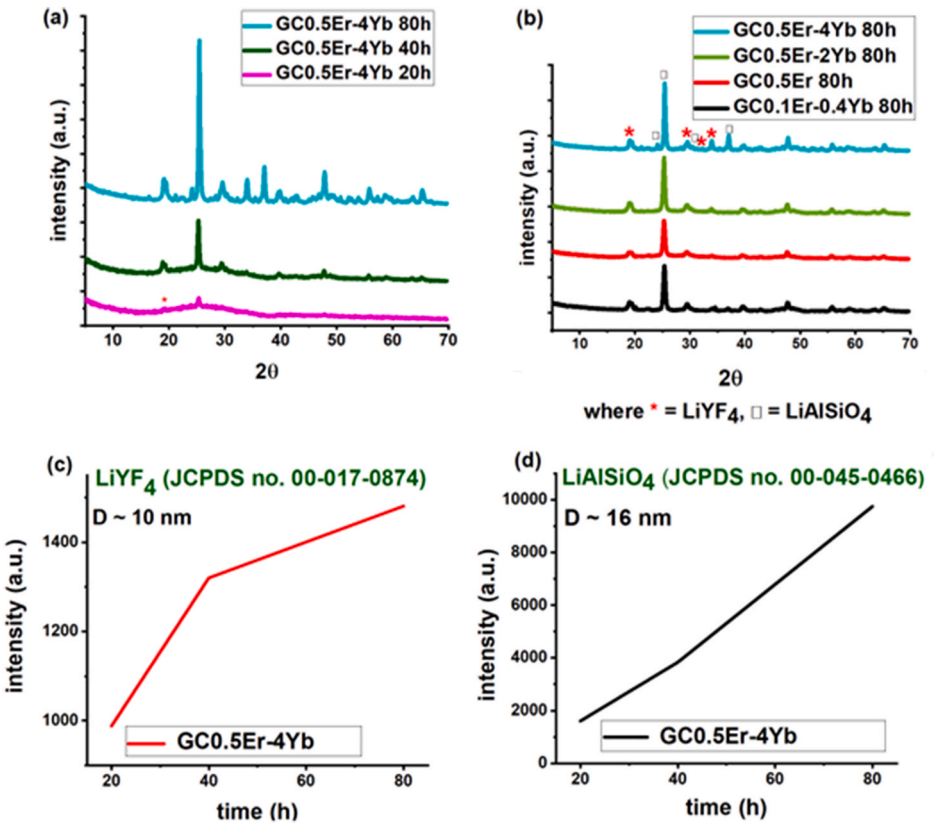

Fig. 2. (a) XRD of GC0.5Er-4Yb at different treatment times at 540 °C, (b) XRD of GCs with different dopant concentrations treated at 540 °C for 80 h. (c) and (d) Intensity of the main diffraction peak of $LiYF_4$ and $LiAlSiO_4$ as a function of treatment time at 540 °C for GC0.5Er-4Yb.

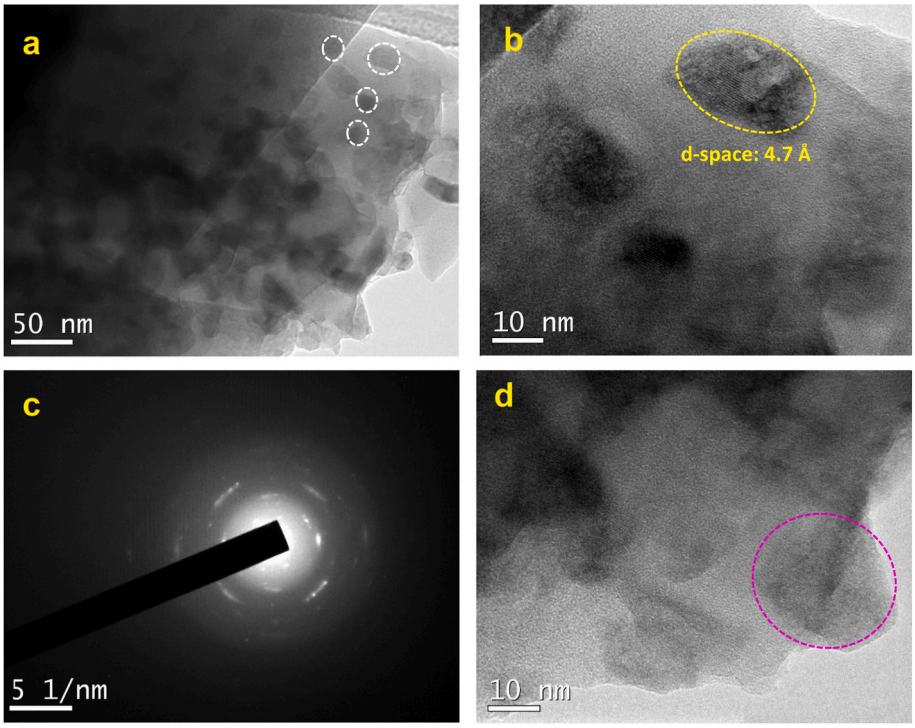

Fig. 3. (a) TEM, (b) HR-TEM, (c) SAED, and (d) EDS analyzed area of GC0.5Er-4Yb after 80 h thermal treatment.

The TEM observation of GC0.5Er-4Yb – 80 h (Fig. 3a) confirmed the crystalline phases observed by XRD, as well as the nanoscales of crystals, less than 20 nm. Fig. 3b depicted a micrograph of high-resolution transmission electron microscopy (HR-TEM) with the presence of several nanocrystals. The d-spacing between adjacent planes were 4.70 Å and 3.07 Å, which corresponded well with the distance between the

(101) and the (112) lattice planes, two strongest signals in $LiYF_4$. Fig. 3c shows the selected area electron diffraction (SAED) which clearly depicted the lattice arrangement of the atoms in the nanocrystals in Fig. 3b. Compared to the above nanocrystal XRD pattern, the calculated lattice parameters from HR-TEM were in agreement with the extracted XRD data and clearly indicated the formation of the body-centered tetragonal $LiYF_4$ phase and corresponded to the indices (hkl) lattice planes as 4.68 and 3.02 Å for the (101) and (112) respectively. In a crystal site with S_4 point symmetry, the dopant ions Er^{3+} and Yb^{3+} replace the Y^{3+} ions.

Additionally, energy-dispersive X-rays spectroscopy (EDS) analysis was operated from the selected area in Fig. 3d to determine the presence of elements in the observed area. The formation of fluoride nanocrystals was reaffirmed by a significant increase in Fluorine % atomic = 36.19% in the crystals relative to its surrounding glass % atomic = 7.59%.

However, the heterogeneous glass matrices and fast moving of NCs recorded by TEM did not allow capturing the morphologies of tetragonal $LiYF_4$ and hexagonal $LiAlSiO_4$ as well as their nanocrystal distribution.

Fig. 4 depicted the optical transmission spectra of doped glasses Gs and their corresponding GCs obtained by heat treatment at various intervals. The doped glass samples exhibited a transmittance of around 90% in both the NIR and visible spectral regions (Fig. 4a). The intense characteristic absorption peaks observed at approximately 1530, 800, 650, 520, 490, and 380 nm corresponded to energy transitions within Er^{3+} ions, whereas the broad characteristic absorption bands at approximately 940 and 980 nm, which increased with Yb concentration, were distinctive features of Yb^{3+} ions [23]. The offsets at 850 nm are caused by changing between two detectors from infrared to visible region. The high absorption cross-section at 980 nm in the Yb^{3+} ion, which acted as an efficient sensitizer by transferring the absorbed energy to the adjacent Er^{3+} ion, was advantageous for pumping Yb and Er ions for upconversion applications. The resulting OxGCs maintained a high level of transparency in the NIR (90%) and visible (70%) windows after 20 h of treatment (Fig. 4b). However, with the increase of heat treatment time (Fig. 4c), the transmittance of GCs tends to decrease as the content of the crystal phase and the size of crystal particles increased during the prolonged treatment period; the scattering effect of light was enhanced, resulting in a reduction of light transmittance.

The up-conversion (UC) emission spectra of all studied glasses and corresponding glass-ceramics were recorded under excitation at 980 nm LD with a power of 500 mW. The UC spectra of parent glasses and their GCs after 20 h treatment are depicted in Fig. 5. Both exhibited characteristic UC emission bands; for glasses, the bands are inhomogeneous broadened, which is typical for Er^{3+} hosted in disordered matrices. The green UC emissions, involving emission bands centered at about 520 nm, 540 and 550 nm, originate from the $^2H_{11/2} \rightarrow {}^4I_{15/2}$ and $^4S_{3/2} \rightarrow {}^4I_{15/2}$ transitions of Er^{3+} ions, respectively. In parent glasses, red UC emissions centered at approximately 650 and 670 nm, which were related to the $^4F_{9/2} \rightarrow {}^4I_{15/2}$ transition of Er^{3+}, predominated over green UC. Moreover, Yb^{3+} ion-containing glasses had a stronger UC luminescence output that increased with Yb^{3+} concentration than glasses containing solely Er^{3+} ions [24,25]. As shown in Fig. 5b, the same trend was observed in GCs. It is worth noting that the UC emission intensity was enhanced, and the Stark splitting was more noticeable for the GC samples compared to the glasses, indicating the incorporation of Er^{3+} and Yb^{3+} ions into the crystalline phase. The low phonon energy owning to the fluoride phase, $LiYF_4$, favored the UC processes after glass crystallization. The UC emission spectra of prepared GCs, which contained $0.5Er^{3+}$ doping, were identical in shape and red/green intensity ratio as reported recently for $LiYF:Er^{3+}$, Yb^{3+} nanocrystals [9,18,22,23] Compared to other samples, GC0.1Er-0.4 Yb-20 h exhibited a greater green intensity than its red counterpart, proven by the decrease in R/G ratio less than 1 as well as the emission shape of its green emission being superior to its red one, which is depicted in Fig. 5b.

The UC emission spectra recorded for glass G0.5Er-4Yb and corresponding GCs prepared by thermal treatment of parent glass at 540 °C at

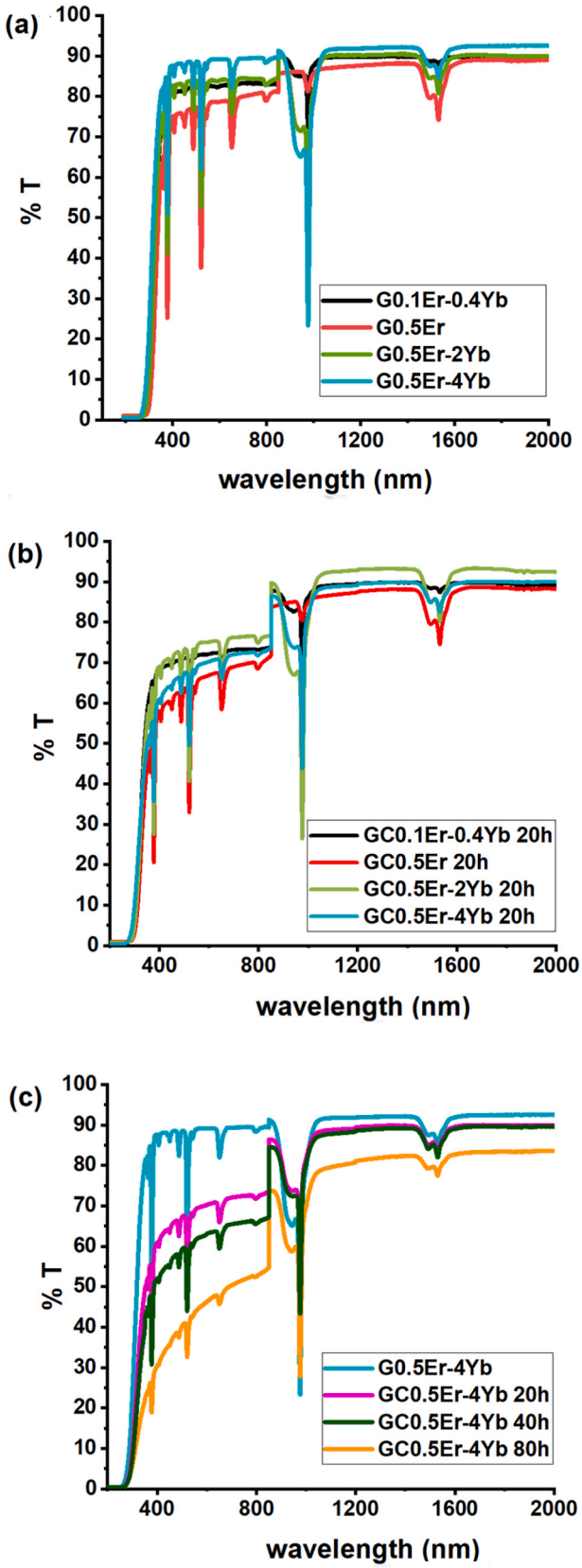

Fig. 4. Transmission spectra of (a) doped-glass samples, (b) their GCs after 20 h treatment, and (c) the parents' glass G 0.5Er-4Yb and its GCs treated at 540 °C, for 20, 40 and 80 h.

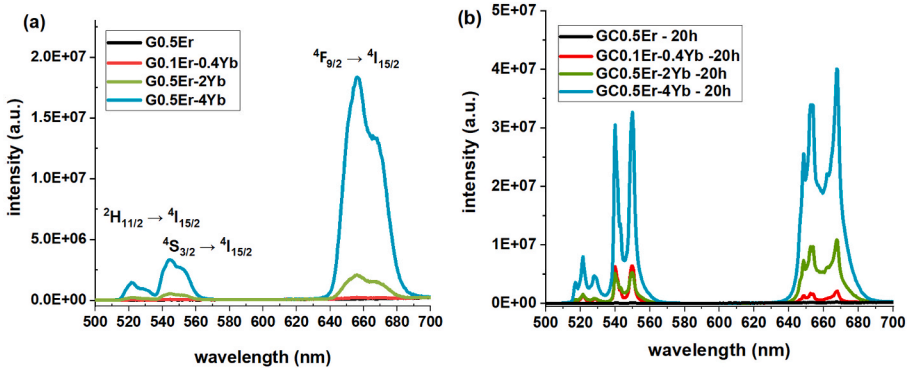

Fig. 5. UC emission spectra of (a) the parent glasses and (b) the corresponding GCs with various dopant concentrations treated at 540 °C for 20 h.

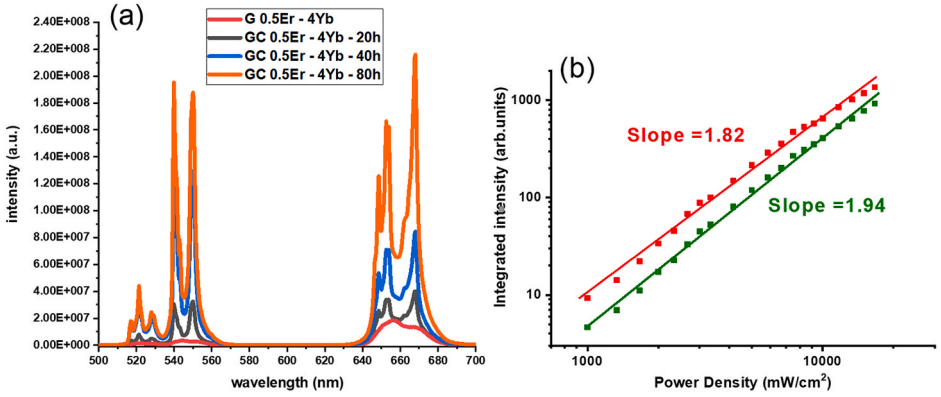

Fig. 6. (a) PL spectra of the GCs treated for 20, 40 and 80 h at 540 °C compared to their parent glass G0.5Er – 4 Yb, and (b) Logarithmic plot of the integrated emission intensities of the upconverted red and green emissions as a function of the 980 nm laser power intensity for GC0.5Er-4Yb-80 h sample. Symbols represent experimental data and solid lines linear fits. (For interpretation of the references to color in this figure legend, the reader is referred to the Web version of this article.)

different dwell times (20, 40, and 80 h) under 980 nm excitation are depicted in Fig. 6a. As the amount of dopants incorporated into the crystal phase increased over time, the intensity of up-conversion increased.

To obtain more information about the UC processes, the dependence of the green and red UC emissions as a function of the incident pump power were studied for selected sample GC0.5Er-4Yb-80 h. It is well known that the UC emission intensity (I_{UC}) depends on the incident pump power (P_{pump}) according to the relation $I_{UC} \propto (P_{pump})^n$, where n is the number of incident photons required for population of the emitting levels. In a double logarithmic plot, UC emission intensity vs. incident pump power, the value of n can be obtained as the slope of this dependence. Fig. 6b shows the logarithmic plot of the UC green and red integrated emission intensities vs. pump power for the glass-ceramic sample GC0.5Er-4Yb after 80 h of thermal treatment. The dependence is nearly quadratic, with n values of 1.94 and 1.82 for green and red emissions, respectively. The obtained values close to 2 indicate that two-photon UC process populates $^4S_{3/2}$ and $^4F_{9/2}$ energy levels. A somewhat lower values (1.50 for green and 1.31 for red emissions) were obtained for the sample GC0.5Er-4Yb thermally treated for 40 h. The lower values of the slope than 2 can be attributed to several processes such as cooperative energy transfer and cross-relaxation or to excitation saturation induced at higher excitation densities.

The UC luminescence mechanism in the codoped glasses and glass-ceramics could be described in Fig. 7 as follows: the excitation of a 980 nm diode laser pumped the ground state of Yb^{3+} and Er^{3+} ions into higher energy levels (Yb^{3+}: $^2F_{7/2} \rightarrow {}^2F_{5/2}$; Er^{3+}: $^4I_{15/2} \rightarrow {}^4I_{11/2}$) through ground state absorption (GSA). However, because Yb^{3+} ions had a much larger absorption cross-section than Er^{3+} ions, the 980 nm photon preferentially populated directly the $^2F_{5/2}$ upper level of Yb^{3+} ions and

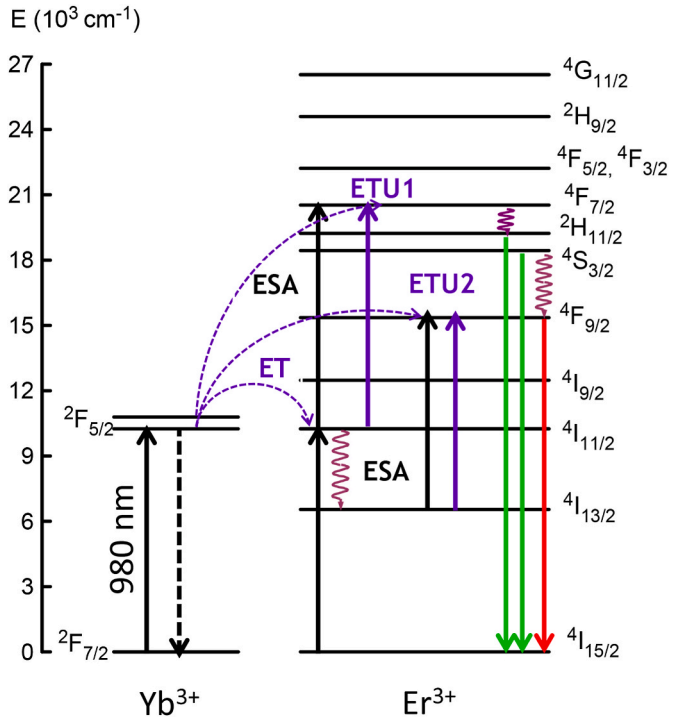

Fig. 7. Simplified energy level diagram and possible populating pathways of codoped materials under 980 nm excitation [14].

subsequently transferred the absorbed energy (energy transfer - ET) to the neighbouring Er^{3+} ion populating the $^4I_{11/2}$ upper level of Er^{3+} ion. Thus, the $^4I_{11/2}$ level of Er^{3+} was mainly populated via ET from Yb^{3+} ions due to their compatible energy matching levels. Then, the populated $^4I_{11/2}$ level absorbed another incident photon via excited state absorption (ESA), reaching the $^4F_{7/2}$ excited state of Er^{3+}. The $^4F_{7/2}$ state could also be populated by energy transfer upconversion (ETU1) from an Yb^{3+} ion ($^2F_{5/2} \rightarrow {}^2F_{7/2}$) ($Yb^{3+}$); ($^4I_{11/2} \rightarrow {}^4F_{7/2}$) ($Er^{3+}$). After non-radiative relaxation from $^4F_{7/2}$ state to the $^2H_{11/2}$ and $^4S_{3/2}$ levels, the green UC luminescence (525 nm and 545 nm) could be emitted via radiative process ($^2H_{11/2}$, $^4S_{3/2}$)$\rightarrow {}^4I_{15/2}$. When referring to the red UC emission ($^4F_{9/2} \rightarrow {}^4I_{15/2}$) at about 650–670 nm, two primary routes are possible: (1) direct population of $^4F_{9/2}$ level through non-radiative transition of $^4S_{3/2}$ (Er^{3+})$\rightarrow {}^4F_{9/2}$ (Er^{3+}) due to multi-phonon relaxation, or (2) population of $^4F_{9/2}$ level from the $^4I_{13/2}$ first excited state, populated by multi-phonon non-radiative relaxation process from $^4I_{11/2}$ (Er^{3+}) level, via ESA $^4I_{13/2}$ (Er^{3+})$\rightarrow {}^4F_{9/2}$ (Er^{3+}) and/or via an energy transfer process described by ($^2F_{5/2} \rightarrow {}^2F_{7/2}$) ($Yb^{3+}$); ($^4I_{13/2} \rightarrow {}^4F_{9/2}$) ($Er^{3+}$) (ETU2).

The integrated intensity ratios of red to green (R/G) emissions for the glass and GC samples were extracted from UC spectra and data were plotted in Fig. 8a. The red intensities in glass samples were approximately 4–6 times greater than the green intensities, indicating that red emission was stronger than green emission. According to calculated R/G ratio, G0.5Er-4Yb and G0.5Er appeared of higher value than G0.5Er-2Yb and G0.1Er-0.4 Yb. Among GC samples, contrary to the increase in the concentration ratio of Yb^{3+} ions to Er^{3+} ions, the R/G emission intensity ratio decreased. This was consistent with previous research on the effect of Yb^{3+} ions on the UC process [18]; the R/G ratio can be altered by varying the concentration of Yb^{3+}ion. By adding Yb^{3+} ions as sensitizers, which have the capacity to absorb excitation light efficiently and transfer photon energy to Er^{3+} ions, the intensity of UC emission was better maximized [24].

As previous stated, the red emission that dominated the UC spectra of Er^{3+}/Yb^{3+}-doped glasses could be clarified in the context of the multi-phonon non-radiative relaxation that was favored in the glasses. The relatively large vibrational energies like Si–O, Si–O–Al bonds (about 1000 cm^{-1}) and possibly also OH groups (about 3500 cm^{-1}) could easily bridge the non-radiative relaxation from $^4I_{11/2}$ to $^4I_{13/2}$ level (approximately 3600 cm^{-1}) and/or from $^4S_{3/2}$ to $^4F_{9/2}$ level (approximately 3000 cm^{-1}). To reveal the mechanism, the PL spectra of glasses (not shown here) were also recorded under 378 nm excitation. The spectra exhibit the dominant green emissions due to the ($^2H_{11/2}$, $^4S_{3/2}$)$\rightarrow {}^4I_{15/2}$ transitions and only very weak bands ($^4F_{9/2} \rightarrow {}^4I_{15/2}$) in the red spectral region. This points to the fact, that $^4F_{9/2}$ state, responsible for the red UC emission ($^4F_{9/2} \rightarrow {}^4I_{15/2}$), is predominantly populated either by the ESA process ($^4I_{13/2}$ + photon $\rightarrow {}^4F_{9/2}$) and/or by energy transfer (ETU2) process denoted as (Yb^{3+}:$^2F_{5/2} \rightarrow {}^2F_{7/2}$):($Er^{3+}$:$^4I_{13/2} \rightarrow {}^4F_{9/2}$), rather than by the multi-phonon assisted relaxation process $^4S_{3/2} \rightarrow {}^4F_{9/2}$. The cross-relaxation processes (e.g. (Er^{3+}:$^4S_{3/2} \rightarrow {}^4I_{13/2}$):($Yb^{3+}$: $^2F_{7/2} \rightarrow {}^2F_{5/2}$)) may also play the role in population of $^4I_{13/2}$ and $^4F_{9/2}$ levels within Er^{3+} ions in co-doped systems. As a result, the multi-phonon assisted relaxation from $^4I_{11/2}$ to $^4I_{13/2}$ level, favouring the population of the $^4F_{9/2}$ state in the Er^{3+} through ESA and/or ETU2 (preferentially) processes, thus enhancing the UC red emission.

The red emission tended to lose its prominence when GCs were formed. After thermal treatment, green emission intensities grew over time, presented in the dropped down of R/G ratio in glass-ceramics samples when compared to their parent's glasses. This decreasing ratio as a function of treatment time indicated that Er^{3+} and Yb^{3+} ions were incorporated into $LiYF_4$ crystals and thus facilitated green emissions. However, these results contradicted the R/G ratio pattern discovered in a previous study using 11 nm $NaYF_4$ hexagonal crystals as host matrices [13]. It could be suggested that UC emissions were affected by the morphology and density of the crystalline structures. For the G0.5Er-4Yb glass and corresponding GCs, the transformation from glass to glass-ceramics resulted in the change in CIE 1931 chromaticity coordinates (calculated from corrected UC spectra) for the G0.5Er-4Yb glass and corresponding GCs (Fig. 6); transition from the red to the green region. This implied that the R/G of GCs containing $LiYF_4$: Er,Yb crystals could be tuned through incubation times as well.

The decay kinetics of the green and red Er^{3+} emissions of selected glasses and GCs have been recorded under direct excitation of the Er^{3+} ions at 376 nm ($^4I_{15/2} \rightarrow {}^4G_{11/2}$). The decay curves are shown in Fig. 9 and corresponding lifetime data are summarized in Table 3. The decay profiles were fitted with a double-exponential fitting function, Eqn. (2), yielding the fit with low residuals,

$$I(t) = A_1\, exp\left(\frac{t}{\tau_1}\right) + A_2\, exp\left(\frac{t}{\tau_2}\right) \quad (2)$$

where τ_1 and τ_2 are the luminescence lifetimes and A_1 and A_2 are the respective weighing parameters. The average experimental lifetime (τ_{exp}) was calculated using the following formula (Eqn. (3)):

$$\tau_{exp} = \frac{A_1\tau_1^2 + A_2\tau_2^2}{A_1\tau_1 + A_2\tau_2} \quad (3)$$

The decay curves of green and red emissions for all measured samples exhibited a non-exponential shape, as clearly seen in Fig. 9. The double-exponential fit of the decay curves provided two decay components, the short and long lifetimes. For green emission, the short decay component in glasses was found in the range of 12–18 μs, while the long lifetime was in the range of 110–160 μs, respectively. When the parent glass G0.5Er-4Yb was compared with its corresponding GCs, the short decay component was significantly increased, and the longer lifetimes were slightly shortened. The red luminescence lifetimes in glass samples were in the range of 140–150 μs and 540–565 μs, respectively, and for corresponding GCs samples, they were somewhat higher compared to G0.5Er-4Yb glass. The similar trend in lifetimes of green/red emissions in glass and corresponding GC was observed by X. Li et al. [20]. The

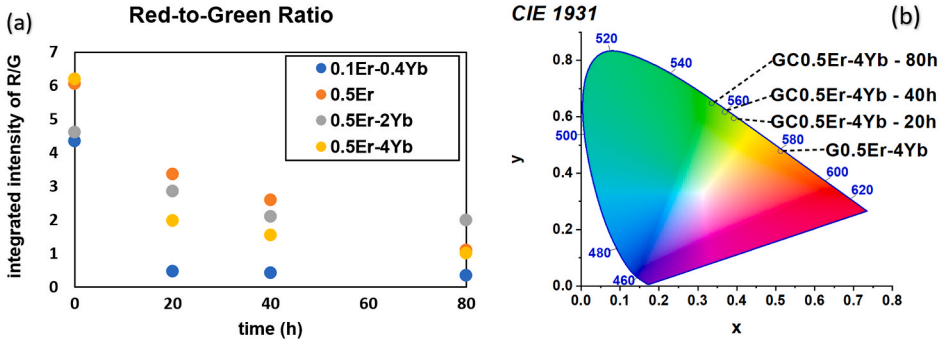

Fig. 8. (a) Red to Green Ratio of all glasses and GCs series, and (b) CIE 1931 chromatogram of G0.5Er-4Yb series. (For interpretation of the references to color in this figure legend, the reader is referred to the Web version of this article.)

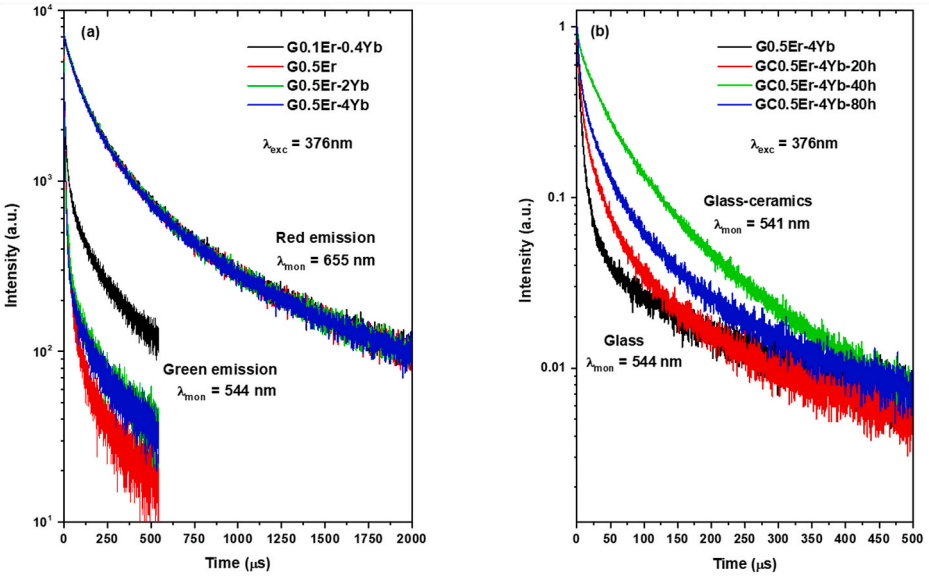

Fig. 9. The decay traces of red and green emission for glasses recorded under direct excitation of 376 nm (a) and green emission of selected glass-ceramic samples treated at 540 °C for incubation time 20, 40 and 80 h. (For interpretation of the references to color in this figure legend, the reader is referred to the Web version of this article.)

Table 3
Lifetime data extracted from double-exponential decay fits of the green and red Er^{3+} emissions for Gs and GCs under direct excitation at 376 nm.

Sample	Green emission (λ_{em} = 544 nm)					Red emission (λ_{em} = 655 nm)				
	τ_1 (μs)	τ_2 (μs)	A_1	A_2	τ_{ave} (μs)	τ_1 (μs)	τ_2 (μs)	A_1	A_2	τ_{ave} (μs)
Glass										
G0.1Er-0.4 Yb	18	160	0.699	0.301	131	147	558	0.756	0.244	374
G0.5Er	14	107	0.913	0.087	53	150	565	0.757	0.243	377
G0.5Er-2Yb	14	138	0.878	0.122	85	144	548	0.754	0.246	368
G0.5Er-4Yb	12	140	0.877	0.123	92	139	540	0755	0.245	363
	Green emission (λ_{em} = 541 nm)					**Red emission (λ_{em} = 653 nm)**				
Glass-ceramics										
GC0.5Er-4Yb-20 h	21	110	0.825	0.175	68	142	554	0.761	0.239	369
GC0.5Er-4Yb-40 h	35	115	0.696	0.304	82	132	519	0.749	0.251	352
GC0.5Er-4Yb-80 h	27	118	0.772	0.228	78	154	581	0.762	0.238	385

interpretation of the decay behavior was however not straightforward when considering the complexity of these GCs. The obtained lifetime values for glasses and GCs reported in this work were however comparable with lifetime data observed for other glass-ceramic systems containing Er^{3+}/Yb^{3+} codoped fluoride nanocrystals [22–25]. As an example, M Secu et al. [26] reported short lifetimes of 15 μs (for 540 nm emission) and 48 μs (for 650 nm emission) for $LiYF_4:Er^{3+},Yb^{3+}$ containing GCs under 378 nm excitation. The reduction of emission lifetimes for the $^4S_{3/2}$ and $^4F_{9/2}$ excited state was attributed to an increase of the non-radiative decay rate due to ions pairing or aggregation that may act as trapping centers and non-radiatively dissipate energy. The lifetime of green emission at 520 nm (λ_{exc} 460 nm) for hydrothermally prepared $LiYF_4:Er^{3+},Yb^{3+}$ nanocrystals calcined at 600 °C was found to be 19 μs and its shortening was associated with surface defects and non-radiative relaxation between the $^4I_{11/2}$ and $^4I_{13/2}$ states [27]. The non-exponential decay of ($^2H_{11/2}$, $^4S_{3/2}$) green emission was also reported for sol-gel derived glass-ceramics with embedded Er^{3+}/Yb^{3+} codoped CaF_2 nanocrystals [28]. The lifetime obtained with a bi-exponential fit was $\tau(^4S_{3/2}) = 7.8$ μs and reduced lifetime value and non-exponential shape of the decay were explained by the efficient cross-relaxation processes between Yb^{3+}-Er^{3+} [$^4S_{3/2}(Er^{3+}) + {}^2F_{7/2}(Yb^{3+}) \rightarrow {}^4I_{13/2}(Er^{3+}) + {}^2F_{5/2}(Yb^{3+})$] and Er^{3+}-Er^{3+} [$^2H_{11/2}(Er^{3+}) + {}^4I_{15/2}(Er^{3+}) \rightarrow {}^4I_{9/2}(Er^{3+}) + {}^4I_{13/2}(Yb^{3+})$] ions, respectively. The decay of $^4F_{9/2}$ level is quasi-exponential with a lifetime $\tau(^4F_{9/2}) = 137$ μs [28]. From the above discussion was clear that several factors may contribute and affect the lifetimes in both glasses and corresponding glass-ceramics.

4. Conclusions

Glasses with nominal compositions of $40SiO_2$–$25Al_2O_3$–$18Li_2O$–$7LiF$–$10YF_3$ doped with ErF_3 and codoped with ErF_3/YbF_3 were prepared by melt-quenching method. As determined by the crystallization kinetics at 540 °C for the four doped glass compositions, the $LiYF_4$ nanocrystals in the related glass-ceramics had scheelite tetragonal morphology and crystal diameters were roundly 10 nm after 80 h' treatment at 540 °C. Another crystallizing phase, $LiAlSiO_4$, which had sizes approximately 16 nm is also present. There was weak UC light emission through the ESA pathway in the singly doped G0.5Er glass and its GCs. However, UC luminescence was enhanced in GCs co-doped with Er^{3+} and Yb^{3+} thanks to the ET pathway, which facilitated the transfer of photons from Yb^{3+} to Er^{3+} especially for the sample G0.5Er-4Yb. The R/G ratio decreased, depicting a shift from red to green after thermal treatment. There were two distinct green emission lifetimes found in G0.5Er-4Yb: a short (12–18 μs) and a long (110–160 μs). The short lifetimes of the GCs were slightly prolonged, while their long lifetimes were reduced. In contrast, the GCs' red emission lifetimes were longer than those of their parent glass. The resulting transparent glass-ceramics

are a promising option for further investigation into optical fiber, lighting devices, and optical thermometry applications.

Funding

This work was supported by a part of the European Union's Horizon 2020 research and innovation program [grant number 739566]; the MICINN [grant number PID2020-115419GBC-21/C-22/AEI/10.13039/501100011033]; and the project VEGA 1/0476/22.

Declaration of competing interest

The authors declare that they have no known competing financial interests or personal relationships that could have appeared to influence the work reported in this paper.

References

[1] A. A de Pablos-Martín, A. Durán, M.J. Pascual, Nanocrystallisation in oxyfluoride systems: mechanisms of crystallisation and photonic properties, Int. Mater. Rev. (2013) 165–186.
[2] M. Rasteiro, T. Gassman, R. Santos, E. Antunes, Crystalline phase characterization of glass-ceramic glazes, Ceram. Int. 33 (2007) 345–354.
[3] L.-D. Sun, H. Dong, P.-Z. Zhang, C.-H. Yan, Upconversion of rare earth nanomaterials, Annu. Rev. Phys. Chem. (2015) 619–642.
[4] E.S.d.L. Filho, K.V. Krishnaiah, Y. Ledemi, Y.-J. Yu, Y. Messaddeq, G. Nemova, R. Kashyap, Ytterbium-doped glass-ceramics for optical refrigeration, Opt Express 23 (2015) 4630–4640.
[5] L.J.Q. Maia, J. Thomas, Y. Ledemi, K.V. Krishnaiah, D. Seletskiy, Y. Messaddeq, R. Kashyap, Photonic properties of novel Yb^{3+} doped germanium-lead oxyfluoride glass-ceramics for laser cooling applications, Front. Optoelectron. 11 (2018) 189–198.
[6] V.K. Kummara, Y. Ledemi, E.S.d.L. Filho, G. Nemova, Y. Messaddeq, R. Kashyap, Development of Yb^{3+}-doped oxyfluoride glass-ceramics with low OH^- content containing CaF_2 nanocrystals for optical refrigeration, Opt. Eng. 56 (2016), 011103.
[7] K.V. Krishnaiah, Y. Ledemi, C. Genevois, E. Veron, X. Sauvage, S. Morency, E.S.d. L. Filho, G. Nemova, M. Allix, Y. Messaddeq, R. Kashyap, Ytterbium-doped oxyfluoride nano-glass-ceramic fibers for laser cooling, Opt. Mater. Express 7 (2017) 1980–1994.
[8] P. Fedorov, A. Luginina, A. Popov, Transparent oxyfluoride glass ceramics, J. Fluor. Chem. 172 (2015) 22–50.
[9] D. Deng, S. Xu, S. Zhao, C. Li, H. Wang, H. Ju, Enhancement of upconversion luminescence inTm^{3+}/Er^{3+}/Yb^{3+}-codoped glass ceramic containing $LiYF_4$ nanocrystals, J. Lumin. 129 (2009) 1266–1270.
[10] W.J. Tropf, M. Thomas, E.W. Rogala, Properties of crystals and glasses, in: M. Bass, C.M. DeCusatis, J.M. Enoch, V. Lakshminarayanan, G. Li, C. MacDonald, V. N. Mahajan, E.V. Stryland (Eds.), Handbook of Optics, 3 ed., vol. 4, The McGraw-Hill Companies, Inc., 2010, p. 72.
[11] M.E. Cruz, M. Sedano, Y. Castro, M.J. Pascual, J. Fernandez, R. Balda, A. Duran, Rare-earth doped transparent oxyfluoride glass-ceramics: processing is the key, Opt. Mater. Express 12 (2022) 3493–3515.
[12] A. de Pablos-Martín, F. Muñoz, G.C. Mather, C. Patzig, S. Bhattacharyya, J. R. Jinschek, T. Höche, A. Durán, M.J. Pascual, $KLaF_4$ nanocrystallisation in oxyfluoride glass-ceramics, CrystEngComm 15 (2013), 10323.
[13] A. de Pablos-Martín, J. Méndez-Ramos, J. del-Castillo, A. Durán, V. Rodríguez, M. Pascual, Crystallization and up-conversion luminescence properties of Er^{3+}/Yb^{3+}-doped $NaYF_4$-based nano-glass-ceramics, J. Eur. Ceram 35 (2015) 1831–1840.
[14] G. Gorni, J.J. Velázquez, M. Kochanowicz, D. Dorosz, R. Balda, J. Fernández, A. Durán, M.J. Pascual, Tunable upconversion emission in $NaLuF_4$–glass-ceramic fibers doped with Er^{3+} and Yb^{3+}, RSC Adv. 9 (2019) 31699–31707.
[15] J. Velázquez, R. Balda, J. Fernández, G. Gorni, G.C. Mather, L. Pascual, A. Durán, M.J. Pascual, Transparent glass-ceramics of sodium lutetium fluoride co-doped with erbium and ytterbium, J. Non-Cryst. Solids 501 (2018) 136–144.
[16] A.A. Cabral, R. Balda, J. Fernández, G. Gorni, J.J. Velázquez, L. Pascual, A. Durán, M.J. Pascual, Phase evolution of $KLaF_4$ nanocrystals and their effects on the photoluminescence of Nd^{3+} doped transparent oxyfluoride glass-ceramics, CrystEngComm 20 (2018) 5760.
[17] Y. Gao, Y. Hu, P. Ren, D. Zhou, J. Qiu, Phase transformation and enhancement of luminescence in the Tb^{3+}-Yb^{3+} co-doped oxyfluoride glass ceramics containing $NaYF_4$ nanocrystals, J. Eur. Ceram. 35 (2016) 2825–2830.
[18] D. Zhang, G. De, L. Zi, Y. Xu, S. Liu, Controlled synthesis and upconversion luminescence properties of $LiYF_4$:$Yb_{0.2}Er_{0.02}$ nanoparticles, MRX 3 (2016), 075005.
[19] G. Lakshminarayana, J. Qiu, Photoluminescence of Eu^{3+}, Tb^{3+} and Tm^{3+}-doped transparent SiO_2-Al_2O_3-LiF-GdF_3 glass ceramics, J. Alloys Compd. 476 (2009) 720–727.
[20] X. Li, L. Qiu, Y. Chen, Y. Zhu, H. Yu, J. Zhong, T. Yang, Q. Mao, $LiYF_4$-nanocrystal-embedded glass ceramics for upconversion: glass crystallization, optical thermometry and spectral conversion, RSC Adv. 11 (2021) 2066–2073.
[21] E. Garcia, R.R. Ryan, Structure of the laser host material $LiYF_4$, Acta Crystallogr. C Struct. Chem. 49 (1993) 2053–2054.
[22] R.D. Shannon, Revised effective ionic radii and systematic studies of interatomic distances in halides and chalcogenides, Acta Crystallogr. A 32 (1976) 751–767.
[23] G.W. Burdick, J.B. Gruber, K.L. Nash, S. Chandra, D.K. Sardar, Analyses of $4f^{11}$ energy levels and transition intensities between Stark levels of Er^{3+} in $Y_3Al_5O_{12}$, Spectrosc. Lett. 43 (2010) 406–422.
[24] X. Chen, L. Jin, W. Kong, T. Sun, W. Zhang, X. Liu, J. Fan, S.F. Yu, F. Wang, Confining energy migration in upconversion nanoparticles towards deep ultraviolet lasing, Nat. Commun. 7 (2016), 10304.
[25] F. Carl, L. Birk, B. Grauel, M. Pons, C. Wurth, U. Resch-Genger, M. Haase, $LiYF_4$: Yb/$LiYF_4$ and $LiYF_4$:Yb, Er/$LiYF_4$ core/shell nanocrystals with luminescence decay times similar to YLF laser crystals and the upconversion quantum yield of the Yb, Er doped nanocrystals, Nano Res. 14 (2021) 797–806.
[26] M. Secu, C. Secu, Up-conversion luminescence of Er^{3+}/Yb^{3+} co-doepd $LiYF_4$ nanocrystals in sol-gel derived oxyfluoride glass-ceramics, J. Non-Cryst. Solids 426 (2015) 78–82.
[27] L. Anbharasi, E. Bhanu Rekha, V. Rahul, B. Roy, M. Gunaseelan, S. Yamini, V. N. Adusumalli, D. Sarkar, V. Mahalingam, J. Senthilselvan, Tunable emission and optical trapping of upconverting $LiYF_4$:Yb,Er nanocrystal, Opt Laser. Technol. 126 (2020), 106109.
[28] S. Georgescu, A.M. Voiculescu, C. Matei, C. Secu, R.F. Negrea, M. Secu, Ultraviolet and visible up-conversion luminescence of Er^{3+}/Yb^{3+} co-doped CaF_2 nanocrystals in sol-gel derived glass-ceramics, J. Lumin. 243 (2015) 150–156.